
Higher-Order Function Networks for Learning Composable 3D Object Representations

Eric Mitchell, Selim Engin, Volkan Isler, Daniel D Lee

Samsung AI Center - New York

{eric.m1,kazim.engin,ibrahim.i,daniel.d.lee}@samsung.com

Abstract

We present a method to represent 3D objects using higher order functions, where an object is encoded directly into the weights and biases of a small ‘mapping’ network by a larger encoder network. This mapping network can be used to reconstruct 3D objects by applying its encoded transformation to points sampled from a simple canonical space. We first demonstrate that an encoder network can produce mappings that reconstruct objects from single images more accurately than state of the art point set reconstruction methods. Next, we show that our method yields meaningful gains for robot motion planning problems that use this object representation for collision avoidance. We also demonstrate that our formulation allows for a novel method of object interpolation in a latent *function* space, where we compose the roots of the reconstruction functions for various objects to generate new, coherent objects. Finally, we demonstrate the coding efficiency of our approach: encoding objects directly as a neural network is highly parameter efficient when compared with object representations that encode the object of interest as a latent vector ‘codeword’. Our smallest reconstruction network has only about 7000 parameters and shows reconstruction quality generally better than state-of-the-art codeword-based object representation architectures with millions of parameters.

1 Introduction

This paper is primarily concerned with the problem of learning efficient 3D object representations. Current learning-based approaches to 3D object representation generally suffer from problems related to memory usage, computational burden, or sampling efficiency. In light of these issues, we propose a functional object representation where an object O is represented as a function $f_{\theta_O} : \mathbb{R}^3 \rightarrow \mathbb{R}^3$ with parameters θ_O that are *unique to that object*. The function is represented as a multilayer perceptron and maps points from a canonical space such as the unit sphere to the set of points defining the object (either the surface or the interior). The parameters of this function are estimated by a ‘higher order’ encoder network g_ϕ , thus motivating the name for our method: *higher order function networks (HOF)*. We compare HOF to two classes of current methods, which we call *direct decoding* and *contextual mapping*, showing that HOF is a generalization of previous contextual mapping methods.

Fundamentally, HOF has two unique features that distinguish it from prior work in 3D object representation learning: *fast-weights encoding* and *function composition as interpolation*.

(1) Fast-weights encoding: Representing an object as the weights and biases of a mapping network. This approach stands in contrast to existing methods which encode objects as vector-valued inputs to a decoder network with fixed weights. Empirically, we find that our approach enables a dramatic reduction (two orders of magnitude) in the size of the mapping network compared to the decoder networks required by other methods.

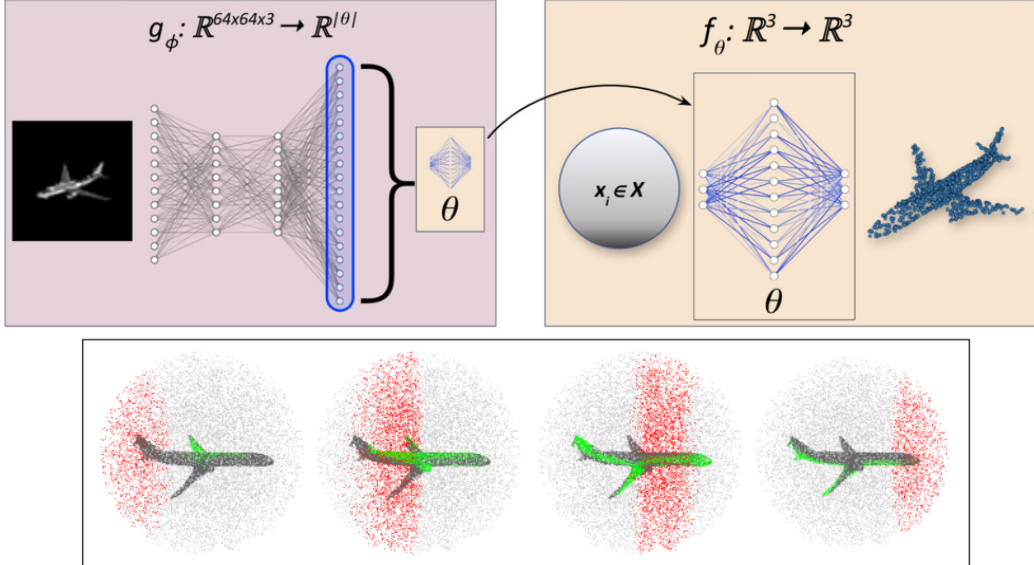


Figure 1: Overview of our method. **Top:** We train a neural network g_ϕ with parameters ϕ (top-left) to output the parameters θ of a mapping function f_θ from an input RGB image (top-right). The function f_θ maps points in \mathbb{R}^3 to points on the 3D model of the object (top-right). **Bottom:** f_θ can be visualized by highlighting different subsets $\tilde{X} \subset X$ (highlighted in red) and their corresponding mapped locations $\{f_\theta(\tilde{x}_i), \tilde{x}_i \in \tilde{X}\}$ (green). Light gray shows $X \setminus \tilde{X}$, dark gray shows entire reconstructed object $\{f_\theta(\mathbf{x}_i), \mathbf{x}_i \in X\}$.

(2) Function composition as interpolation: Our functional formulation enables interpolation between inputs by composing the roots of our reconstruction functions. This method for interpolation differs from existing work, which primarily uses linear interpolation of latent feature vectors (the inputs to a decoder function) to interpolate between objects.

In order to demonstrate the effectiveness of this representation framework, we train HOF on the task of 3D reconstruction from an RGB image using a subset of the ShapeNet dataset [1], showing that it outperforms existing methods in terms of the commonly used Chamfer distance metric. We also evaluate HOF for a motion planning application where the objective is to navigate around an object whose image from the initial location is given. In order to compare object reconstruction methods, we generate a 3D model using this input image and plan a shortest path around the model with the A* algorithm. Experiments indicate that using reconstructions produced by HOF for path planning yields shorter and safer paths.

2 Related Work

In purely geometric terms, an object O is just a subset of \mathbb{R}^3 . Directly representing this infinite set of points in memory, however, is not straightforward. Voxel-based approaches use a uniform discretization of this set in order to extend the highly successful convolutional neural network (CNN) based approaches to the 3D world. However, the inherent sparsity of 3D surfaces make voxelization inefficient in terms of both memory and computation time [2] [3]. Partition-based approaches such as octrees address the space efficiency shortcomings of voxelization, but they are tedious to implement and inefficient to query [4]. Point set representations, discrete and finite subsets of O , have also gained popularity due to the fact that they retain the simplicity of voxel based methods while eliminating their storage and computational burden. The PointNet architecture [5] was a significant milestone in applying deep learning to point cloud representations (although PointNet is concerned with *processing*, rather than *generating*, point clouds). Although point clouds are more flexible than voxels, it is still not obvious how to adapt them to the task of producing arbitrary- or varied-resolution predictions. Functional representations address this issue by representing O as a function f , which

can be manipulated directly and sampled as needed. The question then becomes that of efficiently representing f .

Current approaches to representation and reconstruction generally follow an encoder-decoder paradigm, where the encoder and decoder learn fixed weights. An image I or set of 3D points in O is encoded into a compressed representation \mathbf{z} in some latent space either with a learned encoder g_ϕ with parameters ϕ or by direct optimization of the latent vector itself with respect to a reconstruction-based objective function [6] [7]. \mathbf{z} is decoded by a learned decoder f_θ with parameters θ into a reconstruction of the input object \hat{O} by one of two methods, which we call *direct decoding* and *contextual mapping*:

1. *Direct decoding*: Decode \mathbf{z} directly into a finite set of points or voxels representing the reconstructed object: $g_\phi(I) = \mathbf{z}$, $f_\theta(\mathbf{z}) = \hat{O}$, $|\hat{O}| \in \mathbb{N}$. Examples of direct decoding are the Point Set Generation network proposed in [8], the 3D-r2n2 network proposed in [2], the Deep Level Set paradigm proposed in [9], and the Efficient Point Set Generation (EPCG) architecture presented in [10].
2. *Contextual mapping*: Map elements of some canonical space X (such as the unit sphere) into \mathbb{R}^3 , using \mathbf{z} as a set of additional contextual input activities for the decoder: $g_\phi(I) = \mathbf{z}$, $\{f_\theta(\mathbf{x}, \mathbf{z}) : \mathbf{x} \in X\} = \hat{O}$. Contextual mapping methods typically combine the latent vector \mathbf{z} with samples from X by concatenating a duplicate of \mathbf{z} to each element $\mathbf{x}_i \in X$. If \mathbf{x}_i is in \mathbb{R}^3 and \mathbf{z} in \mathbb{R}^d , and f_θ is an MLP, the input to f_θ is a $(d + 3)$ -dimensional vector. Examples of this approach are the ‘folding’ operation proposed in [11] and the Deep Signed Distance Function [6]. Some approaches, like [12], condition directly on the input, skipping the step of estimating a latent representation \mathbf{z} .

Direct decoding methods generally suffer from the limitation that their predictions are of fixed resolution; they cannot be sampled more or less precisely. With contextual mapping methods, it is possible in principle to sample the entire O with the correct f_θ . However, sampling can provide a significant computational burden for some contextual mapping approaches [6] [9], requiring post-processing such as applying the Marching Cubes algorithm [13]. We show that contextual mapping as described above is a special case of our more general approach, which is based on the ‘fast-weight’ paradigm introduced in [14] and more recently developed in [15]. ‘Fast-weights’ in this context generally refers to methods that use network weights that are not fixed; at least some of weights are estimated on a per-sample basis.

3 Method

3.1 Overview

The object representation that we propose is characterized by a mapping function f_θ that maps a canonical set X , such as the interior of the unit sphere, to the set of 3D points that define the surface or interior of an object O . The mapping function is represented by a multilayer perceptron (MLP). The challenge thus lies in estimating ‘good’ parameters θ for a given input.

We use Higher Order Function (HOF) networks, in which we use an encoder g_ϕ , a convolutional neural network that estimates the parameters of the mapping function f_{θ_I} for an input RGB image I . Our approach is not limited to images; using an encoder architecture like PointNet [5] enables encoding of partial point clouds, for example. In our formulation, in contrast to the direct decoding and contextual mapping methods mentioned previously, the output of our mapping network is modulated by simply changing the connection strengths within the network. This formulation is motivated by the independent observations in both [11] and [6] that using the latent representation \mathbf{z} as context by concatenating it with each member of the canonical input set X in the first layer of f_θ is insufficient for achieving expressive reconstructions, which required architectural workarounds to produce sufficient performance on reconstruction tasks.

Next, we describe in more detail our representation and our methodology for achieving the composability property.

3.2 A Fast-Weights Approach to 3D Object Representation and Reconstruction

We consider the task of reconstruction of an object O from an image I . We consider 64×64 RGB images in the following discussion, but our method is general to any input representation for which a corresponding differentiable encoder network can be constructed to estimate θ . For an input image I , we compute the parameters of the mapping network θ_I as

$$\theta_I = g_\phi(I) \quad (1)$$

That is, the encoder $g_\phi : \mathbb{R}^{3 \times 64 \times 64} \rightarrow \mathbb{R}^d$ directly regresses the d -dimensional parameters θ_I of the mapping network $f_{\theta_I} : \mathbb{R}^c \rightarrow \mathbb{R}^3$, which maps c -dimensional points in the canonical space X to points in the reconstruction \hat{O} . We then transform our canonical space X with f_{θ_I} :

$$\hat{O} = \{f_{\theta_I}(\mathbf{x}) : \mathbf{x} \in X\} \quad (2)$$

This construction allows for higher- or lower-resolution sampling of the reconstructed object in an on-line fashion by continually sampling points from X as desired. In this work, X corresponds to points within the unit sphere in \mathbb{R}^3 , that is: $X = \{\mathbf{x} : \|\mathbf{x}\|_2 \leq 1\}$. However, we have found that the performance of HOF is not very sensitive to the choice of X ; sampling from the surface of the unit sphere in \mathbb{R}^3 or the interior of a 512-dimensional unit hypercube yielded similar-quality reconstructions.

During training, we sample an image I and corresponding ground truth point cloud model \tilde{O} , where \tilde{O} contains 10,000 points sampled from the surface of the true object O . We then obtain the mapping $\hat{f}_{\theta_I} = g_\phi(I)$ and produce an estimated reconstruction of O as in Equation 2. However, we only compute $f_{\theta_I}(\mathbf{x})$ for a sample of 1000 points in X (which is uncountably infinite). This sample is drawn from a uniform distribution over the set. We then compute a loss for the prediction \hat{O} using a differentiable set similarity metric such as Chamfer distance or Earth Mover’s Distance to compute a loss. For the remainder of this paper, we primarily focus on the Chamfer distance as both a training objective and metric for assessing reconstruction quality. The asymmetric Chamfer distance $C(X, Y)$ is a quasimetric often used for quantifying the similarity of two point sets X and Y and is given as

$$C(X, Y) = \frac{1}{|X|} \sum_{\mathbf{x}_i \in X} \min_{\mathbf{y}_i \in Y} \|\mathbf{x}_i - \mathbf{y}_i\|_2 \quad (3)$$

We train g_ϕ to minimize the *symmetric* objective function $\ell(\hat{O}, O) = C(\hat{O}, O) + C(O, \hat{O})$ as in [8].

3.3 Composition as Interpolation

Given our representation of 3D objects as functions, it is natural to inquire into the properties of these functions. We propose an extension of the formulation in Equation 2, where an object is represented as the k -th power of the mapping f_{θ_I} :

$$\hat{O} = \{f_{\theta_I}^k(\mathbf{x}) : \mathbf{x} \in X\} \quad (4)$$

where f^k is defined as the composition of f with itself $(k - 1)$ times: $f^k(\mathbf{x}) = f(f^{(k-1)}(\mathbf{x}))$. We call a mapping f_{θ_I} whose k -th power reconstructs the object O in image I the k -mapping for O .

This modification to Equation 2 adds an additional constraint to the mapping: the domain and codomain must be the same. However, evaluating powers of f leverages the power of weight sharing in neural network architectures; for an MLP mapping architecture with l layers, evaluating its k -th power is equivalent to an MLP with $(l - 1) \times k$ layers with shared weights, which is equivalent to a recurrent neural network with weight sharing in time. This formulation also has connections to earlier work on continuous attractor networks as a model for encoding memories in the brain [16].

We consider the setting in which we have acquired RGB images I and J of two objects, O_I and O_J , respectively. Applying our encoder to these images, we obtain k -mappings f_{θ_I} and f_{θ_J} , which have parameters $\theta_I = g_\phi(I)$ and $\theta_J = g_\phi(J)$, respectively. We hypothesize that we can acquire ‘interpolations’ between the two objects by evaluating any of the 2^k possible functions of the form:

$$f_{\text{interp}} = (f_{\theta_1} \circ \dots \circ f_{\theta_k}) \quad (5)$$

where the parameters of each mapping f_{θ_i} are either the parameters of f_{θ_I} or f_{θ_J} . Key to this procedure is the assumption that the functions f_{θ_I} and f_{θ_J} encode *high-level* information about the underlying structures; without this assumption, interpolating in this way might yield the same results as simply interpolating along some bijection between the two sets O_I and O_J that appeared in I and J . Figures 3 and 6 show that interpolation with function composition provides interesting, meaningful outputs.

3.4 Comparing with Other Methods

We contrast our mapping approach with contextual mapping methods that use a decoder function represented by a neural network with *fixed* weights, such as DeepSDF [6] and FoldingNet [11]. These techniques modulate the output of the decoder through the concatenation of a latent ‘codeword’ vector with each input $\mathbf{x} \in X$. We call this regime the *latent vector concatenation (LVC)* regime, a common manifestation of contextual mapping methods in recent literature. We consider the case in which the latent vector is only concatenated with inputs in the first layer of the decoder network f_θ , which we assume to be an MLP:

If the vector \mathbf{a} contains the pre-activations of the first layer of f_θ , we have

$$\mathbf{a}_I^1 = W^{\mathbf{x}}\mathbf{x} + W^{\mathbf{z}}\mathbf{z} + \mathbf{b}$$

where $W^{\mathbf{x}}$, $W^{\mathbf{z}}$, and \mathbf{b} are fixed, and only \mathbf{z} is a function of I . If we absorb the parameters $W^{\mathbf{z}}$ and \mathbf{b} into ϕ , we can define a new, equivalent latent representation $\mathbf{b}^* = W^{\mathbf{z}}\mathbf{z} + \mathbf{b}$. This gives

$$a_I^1 = W^{\mathbf{x}}\mathbf{x} + \mathbf{b}^*$$

Thus the LVC approach is equivalent to estimating a *subset* of the parameters of the decoder f_θ on a per-sample basis. From this perspective, HOF is an intuitive generalization: rather than estimating some (potentially arbitrarily chosen) subset of θ on a per-sample basis, we might allow our encoder to *learn* which parameters in the decoder f_θ should be fixed, and which should vary per-sample. Theorem 1 in Supplementary Section B formalizes this intuition.

4 Evaluation: 3D Model Reconstruction

4.1 Task & Metric

We test HOF’s ability to reconstruct an object O given a single RGB image of the object using the asymmetric Chamfer distance metrics (Equation 3) as reported in [10]. We evaluate HOF on a subset of the ShapeNet dataset including 13 classes, as initially reported in [17] and later in [10]. The dataset contains 31773 ground truth point cloud models for training/validation and 7926 for testing. For each point cloud, there are 24 RGB renders of the object from a canonical set of 24 camera positions. For both training and testing, each point cloud is shifted so that its bounding box center is at the origin. At test time, there is **no post-processing performed on the predicted point cloud**.

4.2 Results

We find that HOF trained and tested as reported in [10] performs better than current state of the art point set reconstruction methods by a wide margin for nearly all classes. See Table 1 for a class-wise breakdown. As discussed further in Section 5.2, learning in a viewer-centric frame can further improve performance.

4.3 LVC Methods: Runtime Performance Comparison

We compare our fast-weights function approximation architecture with the architecture proposed in [6]. Supplementary Figure 7 shows the full results of this experiment, which measures how long it takes for each network to map a set of N samples from the canonical space X into the object reconstruction (ignoring the processing time for estimating the latent state \mathbf{z} for DeepSDF and the function parameters θ for HOF; we use the same network for both). We find that even for medium-resolution reconstructions ($N > 1000$), the GPU running times for the DeepSDF architecture and HOF begin to diverge. This difference is even more extreme in the CPU running time comparison

Table 1: Class-weighted asymmetric Chamfer distance results for our method compared to other recent methods for 3D reconstruction from images as reported in [10]. We use the HOF-3 architecture 1-mapping.

| Category | 3D-R2N2 [2] | PSG [8] | EPCG [10] | HOF |
|-------------|----------------------|---------------|----------------------|----------------------|
| Airplane | 2.399 / 2.391 | 1.301 / 1.488 | 1.294 / 1.541 | 0.936 / 0.723 |
| Bench | 2.323 / 2.603 | 1.814 / 1.983 | 1.757 / 1.487 | 1.288 / 0.914 |
| Cabinet | 1.420 / 2.619 | 2.463 / 2.444 | 1.814 / 1.072 | 1.764 / 1.383 |
| Car | 1.664 / 3.146 | 1.800 / 2.053 | 1.446 / 1.061 | 1.367 / 0.810 |
| Chair | 1.854 / 3.080 | 1.887 / 2.355 | 1.886 / 2.041 | 1.670 / 1.147 |
| Display | 2.088 / 2.953 | 1.919 / 2.334 | 2.142 / 1.440 | 1.765 / 1.130 |
| Lamp | 5.698 / 7.331 | 2.347 / 2.212 | 2.635 / 4.459 | 2.054 / 1.325 |
| Loudspeaker | 2.487 / 4.203 | 3.215 / 2.788 | 2.371 / 1.706 | 2.126 / 1.398 |
| Rifle | 4.193 / 2.447 | 1.316 / 1.358 | 1.289 / 1.510 | 1.066 / 0.817 |
| Sofa | 2.306 / 3.196 | 2.592 / 2.784 | 1.917 / 1.423 | 1.666 / 1.064 |
| Table | 2.128 / 3.134 | 1.874 / 2.229 | 1.689 / 1.620 | 1.377 / 0.979 |
| Telephone | 1.874 / 2.734 | 1.516 / 1.989 | 1.939 / 1.198 | 1.387 / 0.944 |
| Watercraft | 3.210 / 3.614 | 1.715 / 1.877 | 1.813 / 1.550 | 1.474 / 0.967 |
| Mean | 2.588 / 3.342 | 1.982 / 2.146 | 1.846 / 1.701 | 1.534 / 1.046 |

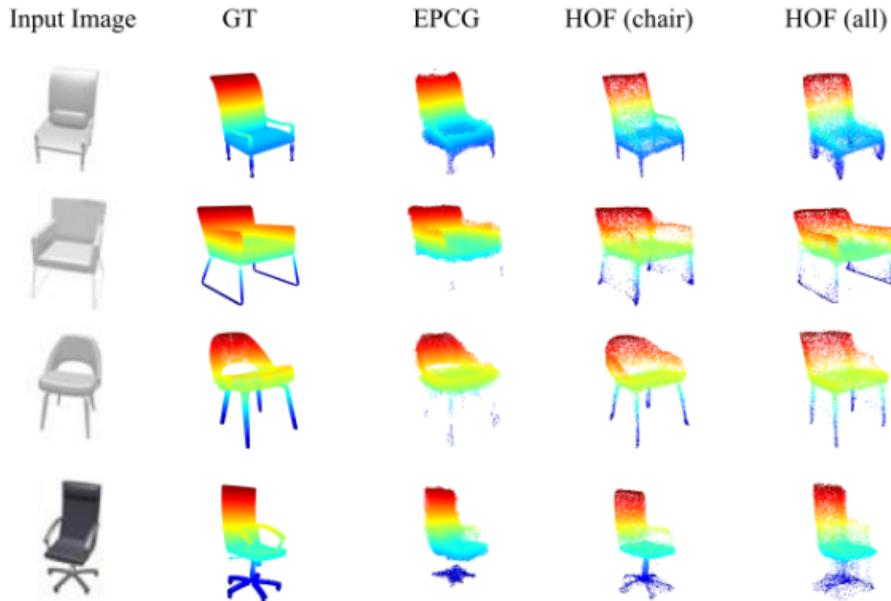


Figure 2: From left to right: Input RGB image, ground truth point cloud, reconstruction from EPCG [10] trained only on chairs, our method trained only on chairs, our method trained on the 13 classes in Table 4.1.

(almost 100x difference). This performance improvement is significant for embedded systems that need to efficiently store and reconstruct 3D objects in real time; our representation is small in size, straightforward to sample uniformly (unlike a CAD model), and fast to evaluate.

4.4 Qualitative Evaluation: Function Composition

To demonstrate the expressiveness of our functional representation, we show that the composition of these functions yields interesting, new objects. If we have estimated 2-mappings for two objects O_A and O_B , we demonstrate that $f_{\theta_A}(f_{\theta_B}(X))$ and $f_{\theta_B}(f_{\theta_A}(X))$ both provide interesting mixtures of the two objects, but *mix the features of the objects in different ways*, i.e. the functions are not commutative. We contrast this approach with other object interpolation methods, which decode

the interpolation of two different latent vectors. In our formulation, we visualize the outputs of an encoder that has been trained to output 2-mappings in \mathbb{R}^3 .

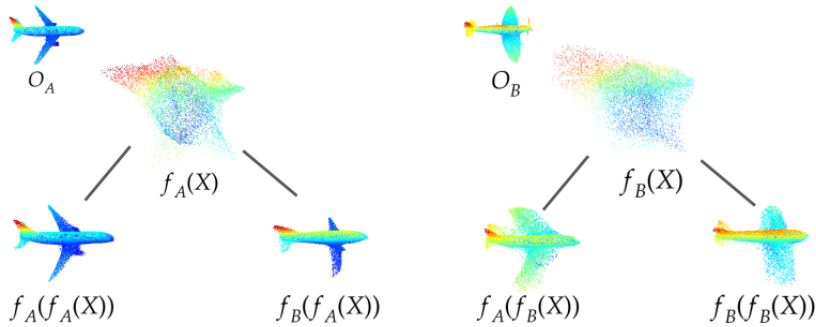


Figure 3: An example of intra-class interpolation between two objects by function composition. We show the ground truth objects O_A and O_B , a single evaluation of their respective decoding functions (giving $f_A(X)$ and $f_B(X)$), as well as the possible permutations of compositions, which makes up the leaf nodes in each tree. In $f_B(f_A(X))$, we see the wings straighten but remain narrow. In $f_A(f_B(X))$, we observe the wings broaden, but they remain angled.

5 Evaluation: Collision-free Path Generation

5.1 Task & Metric

From Chamfer distance scores alone, it is difficult to determine if one method’s reconstruction quality is meaningfully different from another’s. In this section, we introduce a new benchmark to evaluate the practical implications of utilizing 3D reconstructions in the context of an example task: collision-free path generation. We compare the reconstructions of HOF with current state of the art point set reconstruction method [10], which was most competitive with HOF in the reconstruction experiment according to the Chamfer distance metric. We show that given an RGB image, we can efficiently find a near-optimal path \hat{P} between two points around the bounding sphere of the object without colliding with it, and without taking a path much longer than the optimal path P^* , where the optimal path is defined as the shortest collision-free path between two given points. A complete definition of the experiment and its implementation are given in Supplementary Section C.2.4.

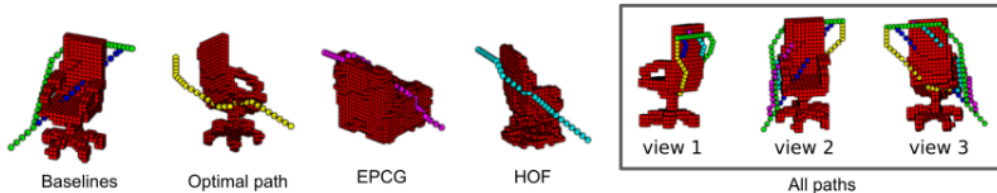


Figure 4: Collision-free path generation. The paths are color-coded as **Blue**: baseline showing L_1 distance, **Green**: baseline going around a bounding box around the object, **Yellow**: with GT voxels as obstacles, **Magenta**: with EPCG voxels, **Cyan**: with HOF voxels. The rightmost figure shows all paths together viewed from three different view points. Best viewed in color.

We quantify the quality of our predictions by measuring both *i*) the proportion of predicted paths \hat{P} that are collision-free and *ii*) the average ratio of the length of a collision-free estimated path \hat{P} and the corresponding optimal path P^* .

These two metrics conceptually mirror the backward and forward Chamfer distance metrics, respectively; a low collision rate corresponds to few missing structures in the reconstructed object (backward Chamfer, or surface coverage), while successful paths close to the optimal path length correspond to few extraneous structures in the reconstruction (forward Chamfer, or shape similarity).

5.2 Results

We find that HOF provides meaningful gains over the reconstruction method recently proposed in [10] in the context of path planning around the reconstructed model. HOF performs significantly better both in terms of path length as well as collision rate. However, although in [10] results were reported on the reconstruction task with objects in a canonical frame, in the context of robotics, learning in a viewer-centric frame is necessary. It has been noted in [18] that generalization might be easier when learning reconstruction in a viewer-oriented frame. We test this theory by training on both objects in their canonical frame as well as in the ‘camera’ frame. We rotate each point cloud Y into its camera frame orientation using the azimuth and elevation values for each image. We rotate the point cloud about the origin, keeping the bounding box centered at $(0,0,0)$. Trained and tested in the viewer-centric camera frame, HOF performs even better than in the canonical frame, giving Chamfer distance scores of $1.486 / 0.979$ (compared with $1.534 / 1.046$ for the canonical frame), a notable improvement. The most notably improved classes in the viewer-centric evaluation is cabinets and loudspeakers; it is intuitive that these particularly ‘boxy’ objects might be better reconstructed in a viewer-centric frame, as their symmetric nature might make it difficult to identify their canonical frame from a single image.

Results of this comparison, as well as other ablation studies, are reported in Supplementary Table 3. The path quality performances of the baseline metrics, EPCG [10] and HOF are presented in Table 2.

Table 2: Mean values for the collision-free path generation success rate and the optimality of the output paths. Higher values indicate better performance. Details about baseline metrics *Shortest L_1* and *Shortest Around Bounding Box (SABB)* are listed in Supplementary Section C.2.4.

| Method | Shortest L_1 | SABB | Efficient PCG [10] | Ours |
|--------------|---------------------------------|---------------------------------|--------------------|------------------------------------|
| Success rate | 0.341 ± 0.35 | 1.0 ± 0.0 | 0.775 ± 0.19 | 0.989 ± 0.06 |
| Optimality | 1.0 ± 0.0 | 0.960 ± 0.05 | 0.994 ± 0.02 | 0.998 ± 0.01 |

6 Conclusion

In this paper, we showed that a 3D object can be efficiently encoded as a function f_θ which maps points in \mathbb{R}^3 to the set of points that define the object. Specifically, we presented *Higher Order Function (HOF)* networks, which take an image of an object as input and generate a function-based representation of the object. The function can be represented as a small multi-layer perceptron with ‘fast-weights’, or weights that are output by an encoder network g_ϕ with learned weights. HOF surpasses state of the art point cloud reconstruction methods in terms of the Chamfer Distance of the output objects to the ground truth. A significant advantage of HOF-based object representations is that the same compact network can be used to generate 3D models of arbitrary resolution by adjusting the density of the input points.

To further evaluate the representation in a task specific manner, we considered the problem of planning paths around objects. HOF-generated models for this task yielded shorter and safer paths as compared to the models generated by the state of the art. Finally, HOF models also provide an intuitive way to interpolate objects by composing the roots of their corresponding mapping functions. To achieve compositionality, we modified HOF to output a mapping f_θ^n , $n > 1$, rather than f_θ , produces accurate reconstructions. This formulation enables interpolation between objects by composing decoder functions estimated from different objects.

For future work, we would like further investigate the richness of our object mapping networks. For example, we would like to better understand the properties of the k -mappings we have described here as well as methods for enforcing properties such as commutativity. Derivatives of HOF might use the function representation directly for example for manipulation or navigation tasks, rather than generating intermediate 3D point clouds. We hope that the work presented in this paper provides a basis for future developments of efficient, composable 3D object representations.

References

- [1] Angel X. Chang, Thomas A. Funkhouser, Leonidas J. Guibas, Pat Hanrahan, Qi-Xing Huang, Zimo Li, Silvio Savarese, Manolis Savva, Shuran Song, Hao Su, Jianxiong Xiao, Li Yi, and Fisher Yu. Shapenet: An information-rich 3d model repository. *CoRR*, abs/1512.03012, 2015. URL <http://arxiv.org/abs/1512.03012>.
- [2] Christopher Bongsoo Choy, Danfei Xu, JunYoung Gwak, Kevin Chen, and Silvio Savarese. 3d-r2n2: A unified approach for single and multi-view 3d object reconstruction. *CoRR*, abs/1604.00449, 2016. URL <http://arxiv.org/abs/1604.00449>.
- [3] Christian Häne, Shubham Tulsiani, and Jitendra Malik. Hierarchical surface prediction for 3d object reconstruction. *CoRR*, abs/1704.00710, 2017. URL <http://arxiv.org/abs/1704.00710>.
- [4] Maxim Tatarchenko, Alexey Dosovitskiy, and Thomas Brox. Octree generating networks: Efficient convolutional architectures for high-resolution 3d outputs. *CoRR*, abs/1703.09438, 2017. URL <http://arxiv.org/abs/1703.09438>.
- [5] Charles Ruizhongtai Qi, Hao Su, Kaichun Mo, and Leonidas J. Guibas. Pointnet: Deep learning on point sets for 3d classification and segmentation. *CoRR*, abs/1612.00593, 2016. URL <http://arxiv.org/abs/1612.00593>.
- [6] Jeong Joon Park, Peter Florence, Julian Straub, Richard Newcombe, and Steven Lovegrove. DeepSDF: Learning continuous signed distance functions for shape representation. *arXiv preprint arXiv:1901.05103*, 2019.
- [7] Jong-Hoon Oh and H. Sebastian Seung. Learning generative models with the up-propagation algorithm. In *Proceedings of the 10th International Conference on Neural Information Processing Systems, NIPS'97*, pages 604–610, Cambridge, MA, USA, 1997. MIT Press. URL <http://dl.acm.org/citation.cfm?id=3008904.3008990>.
- [8] Haoqiang Fan, Hao Su, and Leonidas J Guibas. A point set generation network for 3d object reconstruction from a single image. In *Proceedings of the IEEE Conference on Computer Vision and Pattern Recognition*, pages 605–613, 2017.
- [9] Mateusz Michalkiewicz, Jhony K. Pontes, Dominic Jack, Mahsa Baktashmotlagh, and Anders Eriksson. Deep level sets: Implicit surface representations for 3d shape inference. *CoRR*, abs/1901.06802, 2019. URL <http://arxiv.org/abs/1901.06802>.
- [10] Chen-Hsuan Lin, Chen Kong, and Simon Lucey. Learning efficient point cloud generation for dense 3d object reconstruction. In *Thirty-Second AAAI Conference on Artificial Intelligence*, 2018.
- [11] Yaoqing Yang, Chen Feng, Yiru Shen, and Dong Tian. Foldingnet: Point cloud auto-encoder via deep grid deformation. In *Proceedings of the IEEE Conference on Computer Vision and Pattern Recognition*, pages 206–215, 2018.
- [12] Lars M. Mescheder, Michael Oechsle, Michael Niemeyer, Sebastian Nowozin, and Andreas Geiger. Occupancy networks: Learning 3d reconstruction in function space. *CoRR*, abs/1812.03828, 2018. URL <http://arxiv.org/abs/1812.03828>.
- [13] William E. Lorensen and Harvey E. Cline. Marching cubes: A high resolution 3d surface construction algorithm. In Maureen C. Stone, editor, *SIGGRAPH*, pages 163–169. ACM, 1987. ISBN 0-89791-227-6. URL <http://dblp.uni-trier.de/db/conf/siggraph/siggraph1987.html#LorensenC87>.
- [14] Jürgen Schmidhuber. Learning to control fast-weight memories: An alternative to dynamic recurrent networks. *Neural Computation*, 4(1):131–139, 1992. doi: 10.1162/neco.1992.4.1.131. URL <https://doi.org/10.1162/neco.1992.4.1.131>.
- [15] David Ha, Andrew M. Dai, and Quoc V. Le. Hypernetworks. *CoRR*, abs/1609.09106, 2016. URL <http://arxiv.org/abs/1609.09106>.

- [16] H. Sebastian Seung. Continuous attractors and oculomotor control. *Neural Networks*, 11(7-8): 1253–1258, October 1998. doi: 10.1016/s0893-6080(98)00064-1. URL [https://doi.org/10.1016/s0893-6080\(98\)00064-1](https://doi.org/10.1016/s0893-6080(98)00064-1).
- [17] Xinchun Yan, Jimei Yang, Ersin Yumer, Yijie Guo, and Honglak Lee. Perspective transformer nets: Learning single-view 3d object reconstruction without 3d supervision. *CoRR*, abs/1612.00814, 2016. URL <http://arxiv.org/abs/1612.00814>.
- [18] Jiajun Wu, Chengkai Zhang, Xiuming Zhang, Zhoutong Zhang, William T Freeman, and Joshua B Tenenbaum. Learning shape priors for single-view 3d completion and reconstruction. In *Proceedings of the European Conference on Computer Vision (ECCV)*, pages 646–662, 2018.
- [19] Gao Huang, Zhuang Liu, and Kilian Q. Weinberger. Densely connected convolutional networks. *CoRR*, abs/1608.06993, 2016. URL <http://arxiv.org/abs/1608.06993>.
- [20] Xavier Glorot, Antoine Bordes, and Yoshua Bengio. Deep sparse rectifier neural networks. In Geoffrey Gordon, David Dunson, and Miroslav Dudík, editors, *Proceedings of the Fourteenth International Conference on Artificial Intelligence and Statistics*, volume 15 of *Proceedings of Machine Learning Research*, pages 315–323, Fort Lauderdale, FL, USA, 11–13 Apr 2011. PMLR. URL <http://proceedings.mlr.press/v15/glorot11a.html>.
- [21] Xiuming Zhang, Zhoutong Zhang, Chengkai Zhang, Josh Tenenbaum, Bill Freeman, and Jiajun Wu. Learning to reconstruct shapes from unseen classes. In *Advances in Neural Information Processing Systems*, pages 2257–2268, 2018.

A Other Visualizations

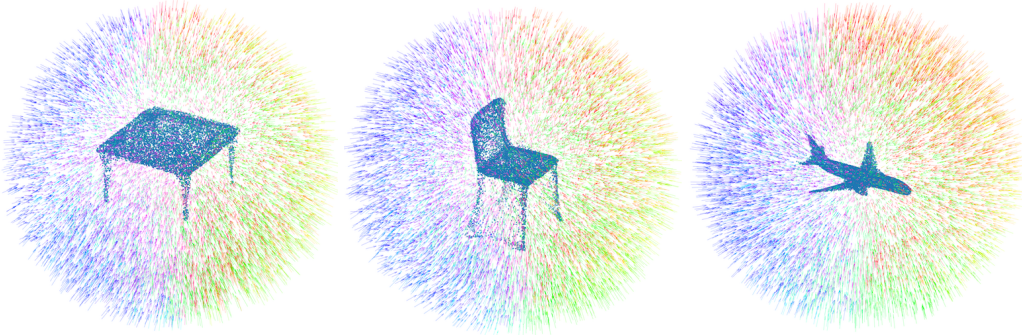


Figure 5: Visualization of the mapping estimated for various objects as the scaled flow direction of each point in the input canonical space X . Vectors are colored according to azimuthal angle.

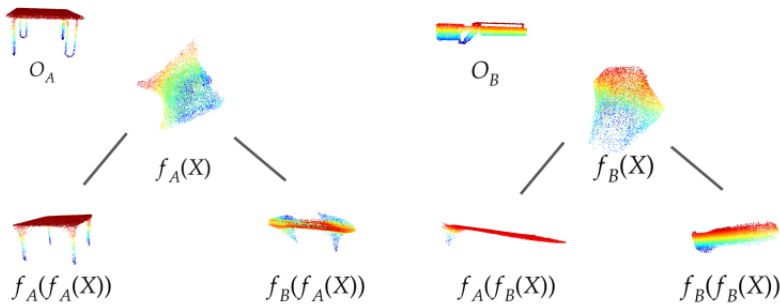


Figure 6: An example of inter-class interpolation, mixing a table and a rifle. We observe what might be interpreted as a gun with legs in $f_B(f_A(X))$ and a table with a single coherent stock in $f_A(f_B(X))$.

B Formal Comparison of HOF and LVC approaches

The observation in Section 3.4 regarding the effect of the codeword \mathbf{z} in the LVC formulation of contextual mapping methods can be formally stated in Proposition 1.

Proposition 1. *If f_θ is an MLP with no skip connections computing outputs as $f_\theta(\mathbf{x}; \mathbf{z}) = f_\theta\left(\begin{bmatrix} \mathbf{z} \\ \mathbf{x} \end{bmatrix}\right)$, \mathbf{z} acts as a bias \mathbf{b} to the first layer pre-activations computed independently for each sample.*

Further, we note that if \mathbf{b} is lower dimensional than \mathbf{z} , there exists infinite \mathbf{z}^* that satisfy $W^z \mathbf{z}^* = W^z \mathbf{z} + \mathbf{b}$. Thus, if the latent vector \mathbf{z} is higher dimensional than the activations in the first layer of f_θ , we see a degeneracy; the additional expressiveness from the higher dimensional \mathbf{z} is wasted.

The HOF regime follows as a generalization of LVC contextual mapping methods when $|\mathbf{b}| < |\theta|$, that is, there are other parameters of the mapping function f_θ other than biases in the first layer. We call this assumption that $|\mathbf{b}| < |\theta|$, where the inequality is strict, our **non-degeneracy assumption** with respect to the architecture of f_θ . Given this assumption, we make a final observation about the expressiveness of the HOF regime in comparison to the LVC regime.

We consider an encoder network g_ϕ whose final layer is fully-connected and a fixed mapping network architecture A_{Map} . We define \mathcal{H} and \mathcal{L} as the spaces of all mapping parameters for architecture A_{Map} that can be estimated from an input image I by the HOF and LVC regimes, respectively, by g_ϕ . Our claim is stated in Theorem 1.

Theorem 1. *Excluding degenerate network architectures according to our non-degeneracy assumption, $\mathcal{L} \subset \mathcal{H}$.*

Proof. $\mathcal{L} \subseteq \mathcal{H}$ follows from Proposition 1 because HOF can compute all parameters in f_θ given an input I while LVC can only compute the first layer biases. To show that the subset is strict, we define two sets of parameters γ and β in \mathcal{H} such that $\gamma = \begin{bmatrix} \mathbf{b} \\ \mathbf{p} \end{bmatrix}$ and $\beta = \begin{bmatrix} \mathbf{b} \\ \mathbf{q} \end{bmatrix}$. $|\mathbf{p}| = |\mathbf{q}| > 0$ by our non-degeneracy assumption. If $\mathbf{p} \neq \mathbf{q}$, γ and β cannot both be in \mathcal{L} because under LVC, parameters in the mapping network other than the first layer bias are fixed. \square

C Training/Testing Dataset and Implementation Details

In the reconstruction experiment, Chamfer Distance scores are scaled up by 100 as in [10] for easier comparison. For the numbers reported in Table 1, we use the best performance of 3d-r2n2 (5 views as reported in [10]). In comparing with methods like FoldingNet [11] and DeepSDF [6], we focus on efficiency of representation rather than reconstruction quality. The performance comparison in Figure 7 and the ablation experiment in Table 3 attempt to compare these architectures in this way (FoldingNet is a slightly shallower version of the DeepSDF architecture; 6 rather than 8 fully-connected layers).

C.1 Dataset

We use the ShapeNet train/validation/test splits of a subset of the ShapeNet dataset [1] described in [17]. Point clouds have 100k points. Upon closer inspection, we have found that this subset includes some inconsistent/noisy labels, including:

1. Inconsistency of object interior filling (e.g. some objects are only surfaces, while some have densely sampled interiors)
2. Objects with floating text annotations that are represented in the point cloud model
3. Objects that are inconsistently small (scaled down by a factor of 5 or more compared to other similar objects)

Although these types of inconsistencies are rare, they are noteworthy. We used them as-is, but future contributions might include both ‘cleaned’ and ‘noisy’ variants of this dataset. Learning from noisy labels is an important problem but is orthogonal to 3D reconstruction.

C.2 Implementation Details

C.2.1 Network Architecture and Training

For the problem of 3D reconstruction from an RGB image, which we address here, we represent g_ϕ as a convolutional neural network based on the DenseNet architecture proposed in [19]. Our encoder network has 3 dense blocks (each containing 4 convolutional layers) followed by 3 fully connected layers. The schedule of feature maps is [16, 32, 64] for the dense blocks. Each fully connected layer contains 1024 neurons.

We use two variants of the mapping architecture f_θ . One, which we call HOF-1, is an MLP with 1 hidden layer containing 1024 neurons. A second version, HOF-3, is an MLP with 3 hidden layers, each containing 128 hidden units. Both formulations use the ReLU activation function [20]. Because g_ϕ and f_θ are all differentiable almost everywhere, we can train the entire system end-to-end with backpropagation. We use the Adam Optimizer with learning rate $1e-5$ and batch size 1, training for 4 epochs for all experiments (1 epoch $\approx 725k$ parameter updates). Training HOF from scratch took roughly 36 hours.

C.2.2 Computing Environment

All GPU experiments were performed on NVIDIA GTX 1080 Ti GPUs. The CPU running times were computed on one of 12 cores of an Intel 7920X processor.

C.2.3 Running Time Comparison

We compare the runtimes of two variants of HOF with the DeepSDF architecture [6] (which is very similar to the FoldingNet architecture in [11], which has 6 hidden layers rather than 8). The results of

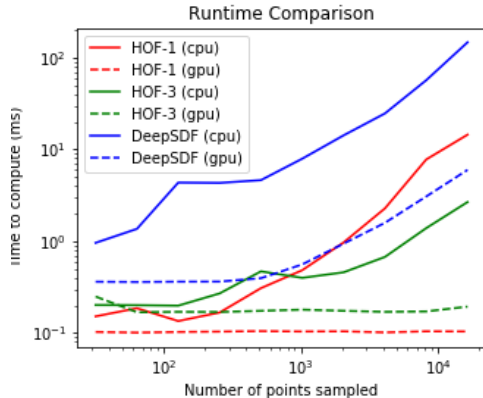


Figure 7: Runtime comparison with the DeepSDF architecture (note the log scales). HOF-1 and HOF-3 are HOF with 1 and 3 hidden layers, respectively. More details about this experiment can be found in the supplement in Section C.2.3.

the comparison can be found in Figure 7. We find that the difference in running time between HOF architectures becomes quite significant as the number of points sampled increases past 10,000 (with DeepSDF taking almost 100 times as long as HOF-1 to map 10,000 points). The exact architectures compared are as follows:

1. HOF-1: 1 hidden layer containing 1024 hidden neurons ($|\theta| = 7171$)
2. HOF-3: 3 hidden layers containing 128 hidden neurons ($|\theta| = 33536$)
3. DeepSDF as described in [6], with 8 hidden layers containing 512 neurons each ($|\theta| \approx 2e6$)

A comparison of the reconstruction quality of different HOF architectures (and different order mappings) can be found in Supplemental Section D. We find that HOF in a variety of different formulations achieves comparable accuracy to the DeepSDF architecture with far fewer parameters and much shorter running time.

C.2.4 Path Planning Experiment

We use the class ‘chair’ from the dataset described in Section 4.1 in our experiments. The objects from this class have considerable variation and complexity in shape, thus they are useful for evaluating the quality of the generated paths.

Path planning is performed in a three dimensional grid environment. All the objects in our dataset fit inside the unit cube. Given the predicted point cloud of an object, we first voxelize the points by constructing an occupancy map $V = n \times n \times n$ centered at the origin of the object with voxel size $2/n$. Next, we generate start and end points as follows. We choose a unit vector \mathbf{v} sampled uniformly at random and compute $\mathbf{d} = n/2 \cdot \mathbf{v}/\|\mathbf{v}\|_1$. We use the end points of \mathbf{d} and $-\mathbf{d}$ as the start and goal locations. For each method, we generate the paths with the A* algorithm by using the voxelization of the predicted point clouds as obstacles, and the sampled start and goal positions. The movement is rectilinear in the voxel space and the distances are measured with the L_1 metric. In the experiments we use an occupancy grid of size $32 \times 32 \times 32$, and sample 100 start and goal location pairs per model.

In addition to the paths generated using the predictions from the EPCG [10] and HOF methods, we present two other baselines (Figure 8). The first baseline *Shortest L_1* outputs the shortest path with the L_1 metric ignoring the obstacles in the scene, and the second baseline *Shortest Around Bounding Box (SABB)* takes the bounding box of the ground truth voxels as the environment to generate the path.

We present the path generation results in Table 2. The baseline *Shortest L_1* gives the optimal solution when the path is collision-free. However, since most of the paths go through the object, this baseline has a poor success rate performance. In contrast, *SABB* output paths are always collision-free as the shortest path is computed using the bounding box of the true voxelization as the obstacles in

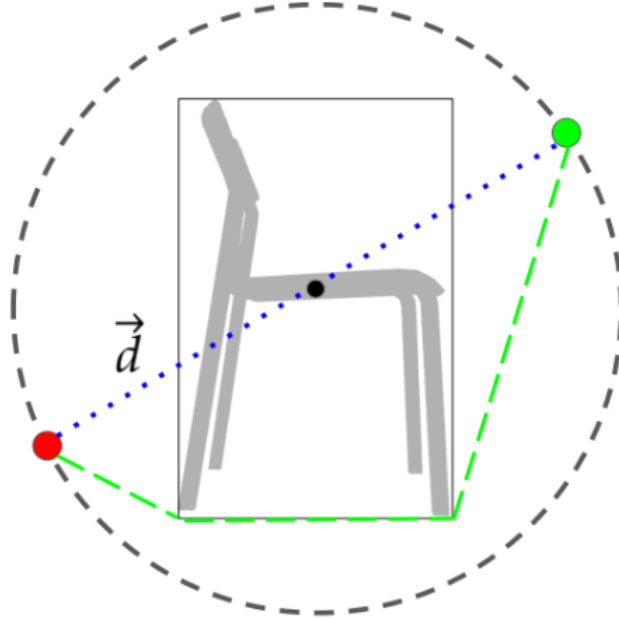


Figure 8: Baseline path generation methods shown in 2D. The dotted path in blue is produced by *Shortest* L_1 and the dashed path in green is by *SABB*. Note that in our experiments we use the rectilinear shortest path as the output of *Shortest* L_1 .

the environment. The length of the paths generated by *SABB* are longer compared to the rest of the methods since the produced paths are ‘cautious’ to not collide with the object. These two baselines are the best performers for the metric they are designed for, yet they suffer from the complementary metric. Our method on the other hand achieves almost optimal results in both metrics due to the good quality reconstructions.

D Ablation Studies

We compare the performance of several variants of HOF on the reconstruction task. First, in Table 3, we compare different training regimes for HOF: canonical frame training (as reported in Table 1), camera frame training, and projection-regularized training.

Table 3: Comparisons of class-weighted asymmetric Chamfer distances of variants of HOF-3 1-mapping.

| Method | Canonical Frame | Camera Frame | Regularized | DeepSDF [6] |
|--------|-----------------|----------------------|---------------|---------------|
| Avg CD | 1.534 / 1.046 | 1.486 / 0.979 | 1.547 / 1.036 | 1.567 / 1.077 |

Projection Regularization Intuitively, we might expect that $f_\theta(X)$ would approximate the Euclidean projection function; e.g. $f_\theta(X) \approx \text{Proj}_Y(X)$. However, qualitatively, we find that without constraining f_θ this is not the case. Figure 9 highlights this distinction. Our mapping f_θ learns a less interpretable mapping from the canonical set X to the object O . In order to encourage the mapping to produce a more interpretable mapping from the canonical set X to the object O , we regularize the transform f_θ to penalize the ‘distance traveled’ of points transformed by f_θ . A regularization term with a small coefficient ($\lambda = 0.01$) is effective in encouraging this behavior, and making this change results in little deviation in performance, while providing a more coherent mapping.

This penalty for the mapping computed by f_{θ_t} for each point in the sample \tilde{X} is given as

$$R(f_{\theta_t}, \tilde{X}) = \frac{1}{|\tilde{X}|} \sum_{\mathbf{x}_i \in \tilde{X}} \|f_{\theta_t}(\mathbf{x}_i) - \mathbf{x}_i\|_2^2 \quad (6)$$

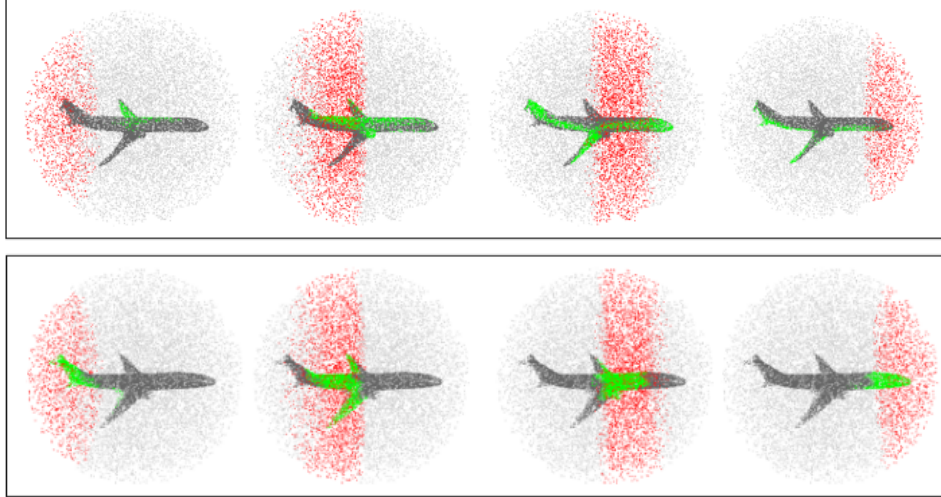


Figure 9: Slices of the sphere where the input points are sampled from and their projections in the predicted point set. **Above:** minimizing the Chamfer distance only. **Below:** Minimizing Chamfer distance with the regularization expression in Equation 6. In both cases, the mapping is smooth, but only with regularization is the mapping close to the intuitive projection mapping.

where \tilde{X} is a sample from the canonical set X . We might instead directly penalize the difference between f_{θ_I} and the Euclidean projection over the sampled set \tilde{X} as:

$$R(f_{\theta_I}, \tilde{X}) = \frac{1}{|\tilde{X}|} \sum_{\mathbf{x}_i \in \tilde{X}} \|f_{\theta_I}(\mathbf{x}_i) - \operatorname{argmin}_{\mathbf{o}_i \in O} \|\mathbf{o}_i - \mathbf{x}_i\|_2\|_2^2 \quad (7)$$

However, we find that this regularization can be overly constraining, for example in cases where points are sampled near the boundaries of the Voronoi tessellation of the target point cloud. The formulation in Equation 6 gives the mapping greater flexibility while still giving the desired semantics.

Camera Frame Prediction We test the hypothesis suggested in [21] that learning reconstruction in a viewer-centric frame generalizes better than a canonical frame. For this experiment, we rotate the ground truth point cloud according to the camera position relative to the object during both training and testing.

Various HOF architectures We compare HOF trained with different architectures and different orders. Results are summarized in Table 4. We find that we achieve state-of-the-art performance across all of the formulations. We also note that for both architectures the 2-mapping outperforms the 1-mapping in forward Chamfer distance, but the 1-mapping outperforms the 2-mapping in backwards Chamfer distance. Future work might investigate the tradeoffs involved in these formulations of the mapping f_{θ} .

Table 4: Comparisons of architectures and mapping orders. We compare HOF-3, 1-mapping, HOF-3, 2-mapping, HOF-1, 1-mapping, and HOF-1, 2-mapping.

| Method | HOF-3 1-mapping | HOF-3 2-mapping | HOF-1 1-mapping | HOF-1 2-mapping |
|--------|-----------------|-----------------|-----------------|-----------------|
| Avg CD | 1.534 / 1.046 | 1.498 / 1.078 | 1.709 / 0.993 | 1.582 / 1.089 |